NANO LETTERS

2007
Vol. 7, No. 12
3739−3746

Removing Structural Disorder from Oriented TiO_2 Nanotube Arrays: Reducing the Dimensionality of Transport and Recombination in Dye-Sensitized Solar Cells

Kai Zhu, Todd B. Vinzant, Nathan R. Neale, and Arthur J. Frank*

National Renewable Energy Laboratory, Golden, Colorado 80401-3393

Received August 24, 2007; Revised Manuscript Received October 11, 2007

ABSTRACT

We report on the influence of morphological disorder, arising from bundling of nanotubes (NTs) and microcracks in films of oriented TiO_2 NT arrays, on charge transport and recombination in dye-sensitized solar cells (DSSCs). Capillary stress created during evaporation of liquids from the mesopores of dense TiO_2 NT arrays was of sufficient magnitude to induce bundling and microcrack formation. The average lateral deflection of the NTs in the bundles increased with the surface tension of the liquids and with the film thicknesses. The supercritical CO_2 drying technique was used to produce bundle-free and crack-free NT films. Charge transport and recombination properties of sensitized films were studied by frequency-resolved modulated photocurrent/photovoltage spectroscopies. Transport became significantly faster with decreased clustering of the NTs, indicating that bundling creates additional pathways via intertube contacts. Removing such contacts alters the transport mechanism from a combination of one and three dimensions to the expected one dimension and shortens the electron-transport pathway. Reducing intertube contacts also resulted in a lower density of surface recombination centers by minimizing distortion-induced surface defects in bundled NTs. A causal connection between transport and recombination is observed. The dye coverage was greater in the more aligned NT arrays, suggesting that reducing intertube contacts increases the internal surface area of the films accessible to dye molecules. The solar conversion efficiency and photocurrent density were highest for DSSCs incorporating films with more aligned NT arrays owing to an enhanced light-harvesting efficiency. Removing structural disorder from other materials and devices consisting of nominally one-dimensional architectures (e.g., nanowire arrays) should produce similar effects.

Semiconductor nanocrystals have been investigated as materials for a wide range of applications, such as solar cells, photoelectrochromics, electroluminescent devices, electronics, sensors, and batteries. For these applications, the forms of nanocrystals—their crystal size, shape, and phase—are critically important. The arrangement of the nanocrystals in the film architecture can also significantly affect the material properties (electrical, optical, chemical, mechanical, etc.). This is especially true for titanium dioxide nanoparticles used in the fabrication of mesoporous films for dye-sensitized solar cells (DSSCs; also known as Grätzel cells).[1] In DSSCs, titania crystallites are covered with dye molecules, and the mesoporous film architecture is interpenetrated with a liquid electrolyte. The crystallite network is the recipient of injected electrons from optically excited dye molecules and provides a conductive pathway to the transparent back contact. Redox species in the electrolyte transport the holes from the oxidized dyes to the counter electrode.

Films normally used for DSSCs have *significant disorder* associated with the individual particles (e.g., defects and size and shape nonuniformities) and the three-dimensional randomly packed particle network having a broad distribution of interconnections.[2,3] Disorder can significantly retard the transport dynamics. For instance, the electron transport is 10^2-10^3 times slower in the mesoporous nanocrystalline films than in single-crystal TiO_2.[4−6] From the light-intensity dependence of the electron diffusion coefficient in TiO_2 nanocrystalline films, it has been inferred that transport is limited by a distribution of localization (waiting) times that electrons spend in traps.[7−13] It has also been shown that with increased film porosity, corresponding to a decrease in the average number of interparticle contacts, the electron transport pathway becomes longer.[2] An important implication of the longer transport pathway is that electrons undergo more trapping and detrapping events and, therefore, spend a longer time in a film before being collected at the electrical contact. Because the collection of photoinjected electrons competes with recombination, high charge-collection efficiencies require that transport is significantly faster than recombination. Thus, the nanostructured architecture is expected to strongly affect the transport and recombination dynamics.[2,3]

* To whom correspondence should be addressed. E-mail: afrank@nrel.gov.

10.1021/nl072145a CCC: $37.00
Published on Web 11/06/2007

One strategy to make electron transport faster in DSSCs is to reduce both the morphological disorder and dimensionality of the network. The utilization of mesoporous films constructed of ordered one-dimensional nanowire[14−17] and nanotube (NT)[18−21] arrays, aligned perpendicularly (vertically) to the electron-collecting substrate, are representative of this approach. Because of the ease of preparing large surface area films of oriented TiO_2 NT arrays by electrochemically anodizing titanium metal,[22] this architecture has attracted considerable interest for use in DSSCs.[18−21] Several studies have shown that the morphology of the arrays (e.g., their pore diameter, intertube spacing, and tube length) can be varied by changing the electrolyte or electrochemical conditions.[22−25] For instance, titania NT arrays can be grown with either irregular or smooth walls depending on whether an aqueous hydrofluoric acid solution[24−26] or a fluoride-containing viscous organic electrolyte[24] is used. Nanotube arrays of greater than 130 μm in length have been produced electrochemically by using a variety of organic electrolytes.[27] As-grown arrays are amorphous and must be transformed to the anatase phase of TiO_2 or subsequently to the rutile phase by heating. Normally, before the as-deposited films are annealed, they are thoroughly rinsed/cleaned with water or some other solvent to remove residual chemicals from the anodization process and then are dried evaporatively in air or under a flow of N_2.

Recently, the transport and recombination properties of oriented NT and nanoparticle films used in DSSCs were studied by frequency-resolved modulated photocurrent/photovoltage spectroscopies.[21] Consistent with intuition, the charge-collection efficiencies were significantly higher in the NT-based DSSCs than in their nanoparticle-based counterparts owing to much slower recombination in the NT films than in the nanoparticle films. Counterintuitively, however, the electron transport times were comparable for both film morphologies, suggesting that some form of disorder limits transport. For example, this disorder could arise from trap states associated with the polycrystallinity of the NT walls[21] or simply from architectural disorder in the films. Clumps of NTs and cracklike features in the films have, in fact, been observed.[28,29] Formation of clusters of bundled NTs in nominally oriented arrays could affect the transport and recombination dynamics in TiO_2 films. Clusters of bundled NTs could be produced during the anodization process[28,29] or, in principle, during the cleaning and evaporative drying process of the as-deposited films through capillary forces of the liquid acting between the NTs. Such capillary forces have the potential to cause not only bundling of NTs but also cracks in the film, depending on, for instance, the surface tension of the liquid and the NT stiffness, aspect ratio, density, and wall thickness. This phenomenon has been observed for materials that are relatively soft in the lateral direction such as silicon nanorods and carbon NT.[30,31] It is, therefore, important to determine the influence of capillary forces, which are likely present during the normal postgrowth cleaning/drying treatment of arrays, on the individual NT structures and film uniformity and their repercussion, if any, on the key operative characteristics governing DSSC performance. Whether produced during the formation of the arrays in the anodization process or by capillary forces in the postgrowth treatment of the as-deposited films, understanding the origin of such orientational disorder and its prevention would be critical for achieving major advances in designing more ordered mesoporous film architectures.

In this work, we examine the morphological effects induced by postgrowth treatment performed on oriented TiO_2 arrays formed from anodized titanium. Capillary forces that arise during evaporative drying of wetted NT films from the postgrowth cleaning step are found to cause clustering of NTs and film cracking, the extent of which depended on the film thickness and surface tension of the cleaning solvent. Eliminating capillary stress during the drying process is shown to result in bundle-free and crack-free films. The structural changes in the films induced by capillary stress alter the spatial dimensionality of the transport and recombination mechanism and the dye-loading capacity. Preventing these changes improves significantly the light-harvesting efficiency and performance of DSSCs.

Titanium foils (Aldrich, 0.25 mm, 99.7% purity) were electrochemically anodized at 20 V versus a Pt counter electrode in a solution of 0.5 wt % NH_4F in glycerol to produce TiO_2 NT arrays with length varying from 1.1 to 6.1 μm.[21,24] After electrochemical anodization, the as-deposited NT films were cleaned by one of three postgrowth treatments. For the first approach (A1), the as-anodized films were cleaned with water and then dried in air; we refer to films prepared by this approach as the water/air-dried NT films. For the second approach (A2), the as-anodized NT films were first cleaned with water, then soaked sequentially in a bath of 20/80, 40/60, 60/40, 80/20, and 100/0 vol % ethanol/water and then dried in air; we denote these films as the ethanol/air-dried NT films. For the third approach (A3), the anodized films were first cleaned with water then soaked sequentially in the bath of 20/80, 40/60, 60/40, 80/20, and 100/0 vol % ethanol/water as described in A2 and then dried using a supercritical CO_2 ($scCO_2$) drying apparatus (SPI-DRY CPD). We refer to these films as the ethanol/$scCO_2$-dried NT films.

After the postgrowth cleaning and drying treatments, the as-deposited amorphous arrays were converted to the TiO_2 anatase phase by annealing at 400 °C in air for 1 h.[21,22] The resulting anatase films were then immersed in 0.3 mM N719 dye (N719 = [tetrabutylammonium]$_2$[Ru(4-carboxylic acid-4′-carboxylate-2,2′-bipyridyl)$_2$(NCS)$_2$]) in ethanol for 24 h and then assembled into DSSCs as detailed before.[32] The amount of adsorbed N719 dye was determined by optical absorption of the desorbed dye.[32] The morphology of NT films was characterized by field emission scanning electron microscopy (SEM) and X-ray diffraction (XRD). SEM images showed that the averages of the NT pore diameters, wall thicknesses, and center-to-center NT distances were 38, 10, and 64 nm, respectively. From these parameters, one can calculate[21] an intertube spacing of 6 nm and a film porosity of 57%. Transport and recombination time constants were measured by intensity-modulated photocurrent spectroscopy (IMPS) and intensity-modulated photovoltage spectroscopy (IMVS) as described previously.[33,34] For these measurements,

the DSSCs were probed with a modulated beam of 680 nm light superimposed on a relatively large background (bias) illumination also at 680 nm. The probe and bias light entered the cell from the counter electrode side. The setup for determining the solar cell characteristics under simulated AM1.5 solar irradiance is discussed elsewhere.[32]

Theory. The capillary force F between two adjacent nanotubes owing to a liquid meniscus can be calculated from

$$F = \frac{1}{2}\pi\gamma (d_o \cos\theta)^2 l^{-1} \quad (1)$$

where γ is the surface tension of the liquid, θ is the contact angle, d_o is the external diameter of nanotube, and $2l$ is the center-to-center distance between nanotubes. Equation 1 was originally derived[35] for two adjacent nanowires with diameter d_o; however, it is applicable to adjacent NTs, where the capillary forces inside the NT pores (with internal diameter d_i) are assumed to have, to a good approximation, zero net contribution to the interactions between nanotubes. The capillary force exerts a bending moment on the NTs, which can cause their deflections, which, in turn, can create bundled NTs and cracks in the films. The maximum lateral deflection δ of a NT resulting from capillary force exerted at the NT's end farthest from the substrate is given by[36]

$$\delta = FL^3/3EI \quad (2)$$

where L is the length (or thickness), E is the Young's modulus, which is a measure of the stiffness of a material, and I is the cross-sectional second moment (also known as the second moment of area), which is a measure of the resistance of an object of a particular shape to bending or deflection. With the aid of the expression[36] $I = \pi (d_o^4 - d_i^4)/64$ and eq 2, the maximum lateral deflection of a NT is described by

$$\delta = \frac{32(d_o \cos\theta)^2 (\gamma L^3)}{3El(d_o^4 - d_i^4)} \quad (3)$$

Equation 3 reveals that deflection depends on the NT geometry and the solvent in contact with NTs. For a fixed d_o, d_i, and l, the extent of deflection of a NT is proportional to γ, L^3, and $(\cos\theta)^2$. Therefore, the larger the surface tension or the longer the NTs, the easier the NTs are deflected by a given capillary force. For the case when a crack (gap) is created by the formation of adjacent domains of bundled NTs with similar maximum lateral deflection, the maximum crack width w_c can be estimated from eq 3 with the expression: $w_c = 2\delta$.

Film Characteristics. Figure 1 shows SEM images of as-deposited (preannealed) NT films, ranging in thicknesses from 1.1 to 6.1 μm, after they were cleaned with water and then dried in air (postgrowth treatment A1). The presence of both clusters of NT bundles and microcracks are evident in even the thinnest films, the 1.1 μm thick film (Figure 1a). When the film thickness increases from 1.1 to 6.1 μm (Figure 1a−c), the extent of bundling and average maximum crack width increases; the average maximum crack widths ($w_c = 2\delta$) increase from roughly 80 to 700 nm. The effect of film thickness on the extent of bundling of NTs and cracks is qualitatively consistent with eq 3, suggesting that the observed deformation is caused by the NT lateral deflection resulting from the action of capillary forces between adjacent NTs during evaporative drying of the wetted films. It can also be seen in Figure 1b,c that an apparent overlayer covers the ends of some channels in the bundled NTs in the thicker films. This overlayer can also be traced to the effect of capillary forces on the bundled NTs during the postgrowth treatment. One consequence of the NT deflection is that the unbalanced capillary forces from both the interior and exterior of pores accelerate the distortion of the pore structure near the ends of the NTs and causes their eventual collapse to produce an overlayer that covers the ends of the opening of the bundled NTs, especially near the center of the bundle in the thicker films.

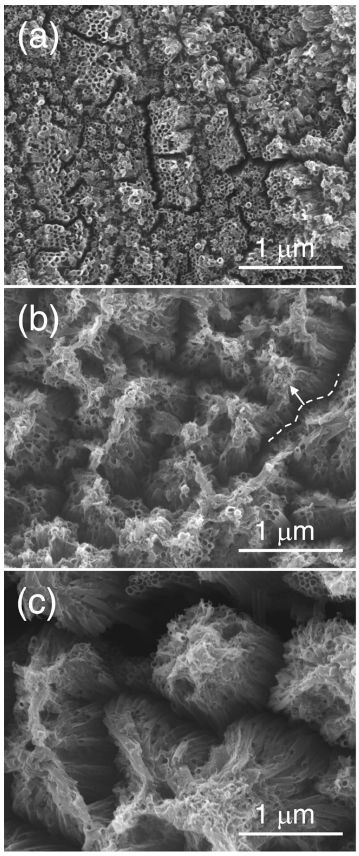

Figure 1. SEM images of (a) 1.1, (b) 2.8, and (c) 6.1 μm thick as-deposited NT films that were cleaned with water and then air-dried (postgrowth treatment A1). The arrow in image (b) denotes a bundle of deflected NTs, and the dashed line marks an associated crack.

Figure 2 shows SEM images of as-deposited NT films that were cleaned with ethanol and then air-dried (post growth treatment A2). The film thicknesses varied from 1.1 to 6.1 μm. It can be seen that the types of morphological disorder (e.g., NT bundles and cracks) in the films are similar to those evident in Figure 1. However, there is a reduced presence of distinct domains of bundled NTs and the associated cracks

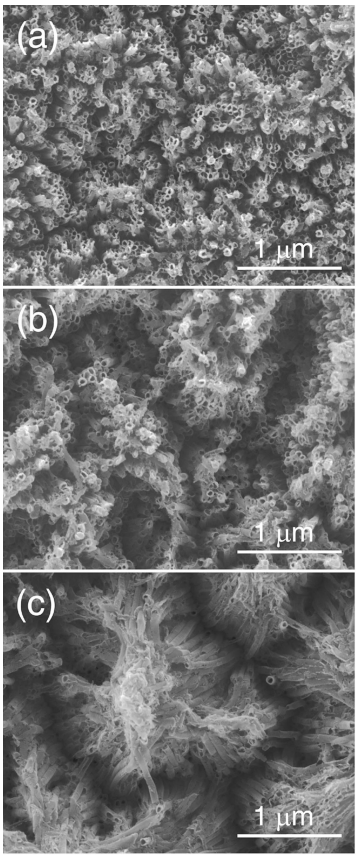

Figure 2. SEM images of (a) 1.1, (b) 2.8, and (c) 6.1 μm thick as-deposited NT films that were cleaned with ethanol and then air-dried (postgrowth treatment A2).

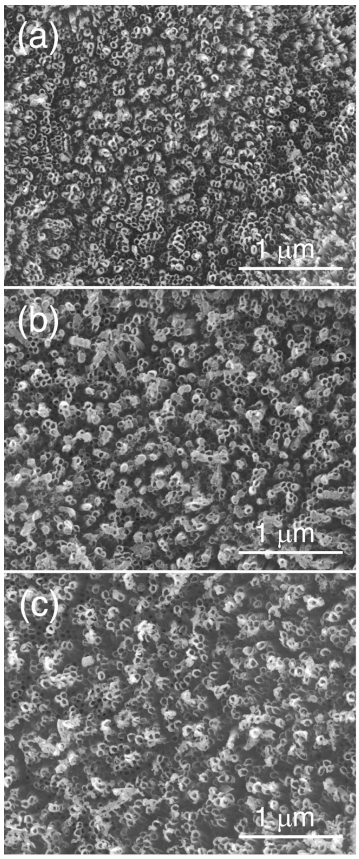

Figure 3. SEM images of (a) 1.1, (b) 2.8, and (c) 6.1 μm thick as-deposited NT films that were cleaned with ethanol and then $scCO_2$-dried (postgrowth treatment A3).

in the 1.1 μm thick film (Figure 2a) compared with the same thickness film (Figure 1a) that was cleaned with water and then air-dried (postgrowth treatment A1). Even in the thicker films (Figure 2b,c), the extent of the formation of bundles, cracks, and overlayer is less than that of the same thickness films (Figure 1b,c) that were washed with water and then air-dried. The reduced degree of morphological disorder in films that were subject to postgrowth treatment A2 rather than postgrowth treatment A1 can be attributed to differences in the surface tension values for water (72 dynes/cm) and ethanol (22 dynes/cm).

Figure 3 shows SEM images of as-deposited NT films with thicknesses ranging from 1.1 to 6.1 μm that were cleaned with ethanol and then dried using the supercritical CO_2 ($scCO_2$) process (postgrowth treatment A3). In its supercritical state, CO_2 passes from the liquid to gaseous phase without crossing the liquid-gas boundary and forming the associated interfacial tension (i.e., $\gamma = 0$ dynes/cm). In the absence of surface tension, there is no evidence of bundles, cracks, or overlayer in the SEM images (Figure 3) of the three films with different thicknesses, consistent with the prediction from eq 3 that NTs should undergo no deflections at $\gamma = 0$ dynes/cm. On the basis of the SEM images in Figures 1−3, we conclude that capillary stress created during evaporation of liquids with nonnegligible surface tension from the mesopores of NT arrays are of sufficient magnitude to induce NT bundling and microcrack formation. Although not investigated in our study, there is also the suggestion[28] that such morphological effects are derived from surface stress created during the growth of the as-deposited films vis-à-vis the anodization and fluoride etching processes. However, because the morphological disorder can be avoided by altering the postgrowth processing, it seems unlikely that disorder arises during the anodization step under our conditions. We note that bundle-free NT samples have been prepared without the use of $scCO_2$.[26,27] The NTs of these samples have, in general, significantly larger dimensions (e.g., 25 nm wall thicknesses[27] and ca. 100 nm tube diameters)[26] than those prepared in the present study. The morphological differences highlight the strong dependence of the degree of tube deflection on the NT physical dimensions (eq 3) as discussed in the Theory section.

The dependence of NT bundles on the film thickness and postgrowth cleaning and drying treatments can be described in terms of an apparent NT deflection δ', defined as the maximum lateral deflection of NTs in a bundle along the associated crack boundary. For example, the dashed line in Figure 1b marks a boundary of a crack, and the arrow denotes a bundle of deflected NTs associated with it. Figure 4 shows the statistical averages (with errors) of NT deflection δ' for as-deposited films cleaned and dried by postgrowth treatments A1 (H_2O/air-dried), A2 (ethanol/air-dried), and A3 (ethanol/$scCO_2$-dried). The average deflection δ' of the NT clusters increases with film thickness in qualitative agreement with the prediction of eq 3.

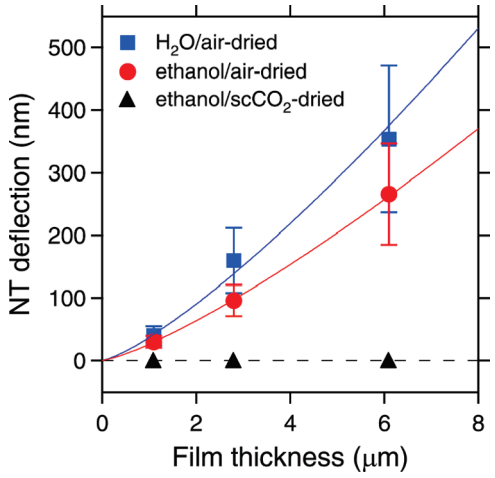

Figure 4. Dependence of NT deflections on film thickness of as-deposited NT films that were subject to postgrowth treatments A1 (H_2O/air-dried), A2 (ethanol/air-dried), and A3 (ethanol/$scCO_2$-dried). The dashed line denotes the case of no deflections of the NTs. Solid lines are best fits to power-law dependences; the best fits of the data yield exponent values within the range of 1.3 ± 0.3.

Quantitatively, the dependence of the average deflection δ' on the film thickness was much less than expected. The average NT deflection δ' of a bundle in as-deposited films that were treated by methods A1 (H_2O/air-dried) and A2 (ethanol/air-dried) increased approximately 9-fold when the film thickness was increased by a factor of 6. Best fits of the data for δ' for methods A1 and A2 treated films (solid lines in Figure 4) can both be represented by the relation $\delta' \propto L^{1.3\pm0.3}$, which is significantly less than the L^3 dependence predicted by eq 3. The underestimation is perhaps not surprising in view of the simplicity of the assumption in deriving eq 3 that lateral deflection of a NT is determined only by the balancing of reactive forces associated with mechanical bending and capillarity. One would anticipate that cooperative interactions of the surrounding structures in the closely packed NT array (the average intertube distance is about 6 nm) would physically constrain the amount of bending movement of individual NTs. Similar capillary effects are reported in a study of Si nanorod arrays,[31] which showed that lateral deflection scales with $L^{1.5}$, in concurrence with the present observation. Despite the more than 3-fold difference in their surface tension values, the deflection values δ' for films treated by methods A1 (H_2O/air-dried) and A2 (ethanol/air-dried) differ by just a factor of 1.4 ± 0.6, which is likely due to the variation in the contact angles of the liquids with TiO_2,[37−39] which partially reduces the effect of surface tension in determining the capillary forces (eq 1).

The effect of capillary stress on the surface area can be estimated by comparing the surface areas of the bundle-free and crack-free ethanol/$scCO_2$-dried films (postgrowth treatment A3) with films treated by method A1 (water/air-dried). The most extreme case of capillary-stress-induced change of surface area would be for films comprised of the longest NTs (namely, the 6.1 μm thick arrays) that were treated by method A1. From dye-desorption measurements, we found 23 ± 13% higher dye-loading in the ethanol/$scCO_2$-dried films than in the H_2O/air-dried films, suggesting that removing morphological disorder induced by capillary stress increased the effective total surface area accessible to dye molecules by 23 ± 13%. The actual surface area of the water/air-dried film could be larger than was measured from dye desorption because the diameter of the dye (ca. 1 nm) restricts its access to some regions within a tightly packed NT bundle. Thus, the 23% increase in surface area represents an upper limit to the difference in the actual surface between the water/air- and ethanol/$scCO_2$-dried films. Not surprisingly, XRD measurements (not shown) indicated that the postgrowth cleaning/drying treatments had no significant effect on the average crystallite size (ca. 30 nm) that comprises the NT walls.

Transport and Recombination. Figure 5 displays typical time constants for transport (τ_c) and recombination (τ_r) as a function of the incident photon flux (light intensity; I_0) for NT-based DSSCs, incorporating 6.1 μm thick annealed TiO_2 films. At this film thickness, the morphological difference in NTs, resulting from postgrowth treatments A1 (water/air-dried) and A3 (ethanol/$scCO_2$-dried), is the largest in this study. Independent of the postgrowth treatments, transport times in both DSSCs (Figure 5a) exhibit essentially the same power-law dependence on the incident light intensity. For randomly packed nanoparticle film-based DSSCs, such power-law dependence is normally attributed to trap-limited transport[7−11] and is described by the expression $\tau_c \propto (I_0)^{\alpha-1}$,[40] where the parameter α describes the shape of the distribution of localization (trapping) times t in the form of $N_T t^{-1-\alpha}$, where N_T denotes the total trap density in the TiO_2 films.[9,40,41] Best fits to the data yield $\alpha = 0.35$ for both water/air- and ethanol/$scCO_2$-dried NTs. Recent studies show that the traps that limit transport in TiO_2 nanoparticle films are located predominantly on the surface of the crystallites and that transport times increase with increasing internal surface area because of the corresponding increase of N_T.[41,42] From the dye-desorption measurements, the average surface area of the ethanol/$scCO_2$-dried film is 23% larger than that of the water/air-dried film. Assuming the density of traps *per unit surface area* is the same for both ethanol/$scCO_2$- and water/air-dried films, an average increase of 23% of the N_T value for the ethanol/$scCO_2$-dried film is expected. According to the relation[40] $\tau_c \propto (N_T)^{2/3}$ at constant illumination and film porosity, electron transport times are expected to be 15% longer on average in the ethanol/$scCO_2$-dried film than in the H_2O/air-dried film. However, despite the larger surface area (larger N_T), it can be determined from Figure 5a that at any given light intensity (e.g., $I_0 = 6.5 \times 10^{16}$ cm^{-2} s^{-1}), the transport times are 43% shorter in the ethanol/$scCO_2$-dried film than in the H_2O/air-dried film. Furthermore, considering the expected 15% difference in transport times resulting from the surface area effect, one can show that if the surface areas were the same (i.e., normalized), the transport times would, in fact, be about 50% shorter in the ethanol/$scCO_2$-dried film than in the H_2O/air-dried film. Or, equivalently, the transport would be about two times faster in the ethanol/$scCO_2$-dried film than in the H_2O/air-dried

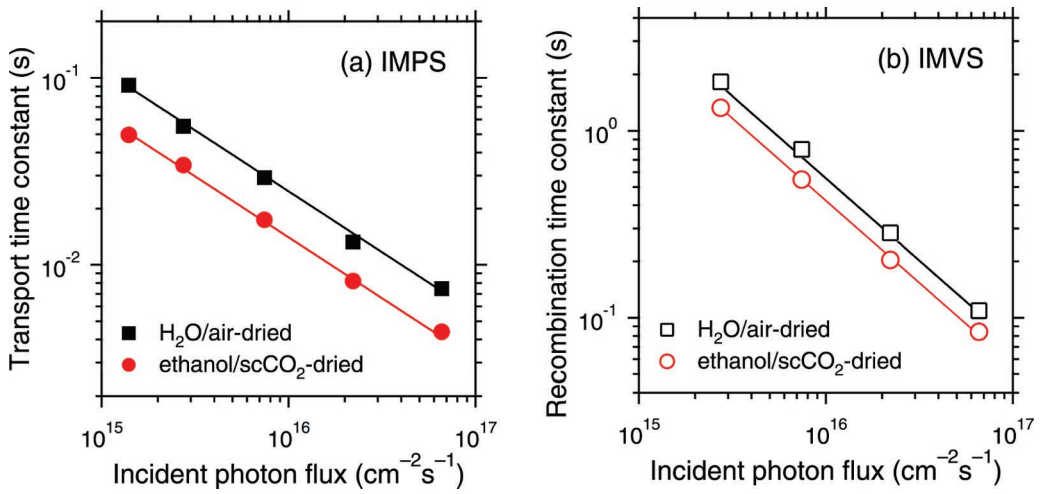

Figure 5. Comparison of the time constants for (a) transport and (b) recombination as a function of the incident photon flux for 680 nm laser illumination for DSSCs, incorporating 6.1 μm thick annealed NT films; preannealed (as-deposited) films were cleaned and then dried by either method A1 (H_2O/air-dried) or method A3 (ethanol/$scCO_2$-dried).

film. So, how can two films with the same parameter α, (normalized) areas, porosities, and thicknesses have different transport times? A reasonable explanation is that the dimensionality of the NT networks differs owing to the intertube contacts created during the formation of NT bundles.

The capillary force exerted on NTs when water (and, presumably, other solvents with appreciable surface tension) is removed by air drying brings adjacent NTs closer together, which, along with the reduction of total surface area, leads to intertube contacts in the bundles of NTs. The formation of intertube contacts would facilitate the lateral charge transport between adjacent NTs in a bundle. Because the collection of electrons at the electrode is determined by the movement of electrons along the length of the NTs, orthogonally to the substrate, lateral movement would slow transport. Creating clusters of intertube contacts in an otherwise one-dimensional network introduces a third spatial dimension to the nominally oriented NT arrays. For an idealized situation in which electrons perform random walks within trap sites that are distributed uniformly in the three-dimensional mesoporous nanoparticle network, the time electrons spend moving along a given direction is one-third of the total time electrons spend moving in all three directions. Thus, transport of charges along a 1-D conducting path would be three times faster than that along a 3-D conducting path. The observation that transport is two times faster in the ethanol/$scCO_2$-dried film than in the water/air-dried film suggests that precluding the formation of NT bundles changes the transport mechanism from a mixture of one and three dimensions to only one dimension. Thus, electrons in a bundle of NT can either move across interconnecting NTs or along the length of a single NT toward the charge-collecting substrate. With higher-dimensional transport systems, the transport pathway becomes longer, resulting in the exposure of electrons to more trap states, the latter of which extends the electrons' residence time in the film before being collected at the electrical contact. The supercritical CO_2 drying process reduces the formation of clusters of bundled NTs, thus promoting 1-D transport, which shortens the transport pathway, lessens the exposure of electrons to traps, and enables overall faster transport.

Figure 5b shows that recombination times are about 23% shorter in ethanol/$scCO_2$-dried NTs than in water/air-dried NTs and exhibit a power-law dependence on the incident light intensity, suggesting a causal connection between transport and recombination. Such a causal link has been observed in TiO_2 nanoparticle-based DSSCs and is attributed to transport-limited recombination.[9,41,43] Recent studies[41] show that the recombination current density scales with (surface area)$^{1.33}$, corresponding to $\tau_r \propto$ (surface area)$^{-0.33}$, at constant film thickness and porosity for TiO_2 nanoparticle films. Considering that the ethanol/$scCO_2$-dried film has a 23% larger surface area than that of the H_2O/air-dried film, one can show that if the surface areas were the same (i.e., normalized), the recombination times would be 18% shorter in the ethanol/$scCO_2$-dried film than in the H_2O/air-dried film. Or, equivalently, the recombination would be 22% faster in the ethanol/$scCO_2$-dried film than in the H_2O/air-dried film. Thus, the effect of the morphological changes on the time constants is significantly smaller for recombination (ca. 18%) than that for transport (ca. 50%), contrary to the prediction of the transport-limited recombination model[41,43] that the recombination times should be proportional to the transport times. In other words, one would expect the recombination times also to decrease by ca. 50% from the base value of the H_2O/air-dried film. This discrepancy between the observation and prediction is attributed, in part, to the creation of additional recombination centers per unit surface area owing to the morphological deformation in the H_2O/air-dried film. We envision that, as the tubes bend to form bundles, the resulting distortion increases the number of surface defects. These additional recombination centers in the H_2O/air-dried film are not present on the straight tubes in ethanol/$scCO_2$-dried film. Thus, recombination in the ethanol/$scCO_2$-dried film is significantly slower relative to the expected value because of the absence of these deforma-

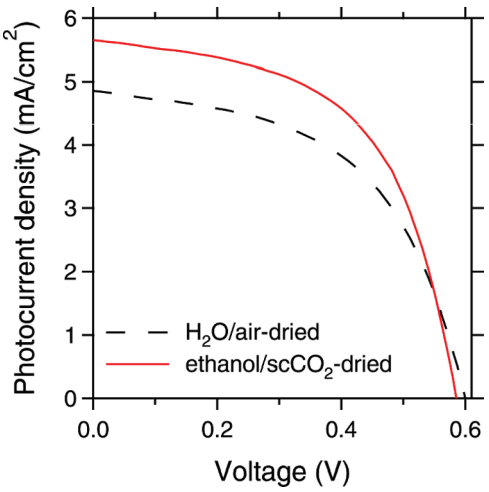

Figure 6. Comparison of $J-V$ characteristics for DSSCs incorporating 6.1 μm thick NT films that were cleaned and then dried by either method A1 (H_2O/air-dried) or method A3 (ethanol/scCO_2-dried). Simulated AM 1.5 light was used.

tion-induced surface defects. From the transport and recombination measurements, one can determine the charge-collection efficiency η_{cc} from the relation $\eta_{cc} = 1 - (\tau_c/\tau_r)$.[10] The values of η_{cc} at constant light intensity (e.g., $I_0 = 6.5 \times 10^{16}$ cm^{-2} s^{-1}; Figure 5) for H_2O/air- and ethanol/scCO_2-dried NT-based DSSCs are 93% and 95%, respectively. If the surface areas were the same (normalized), one can show that η_{cc} for ethanol/scCO_2-dried DSSC would be 3% higher than that for the H_2O/air-dried DSSCs. Thus, removing structural disorder from NT films increases only modestly the charge-collection efficiency. In much thicker films for which the transport and recombination times become more comparable, the formation of NT bundles and microcracks would likely have a much larger effect on the charge-collection efficiency for DSSCs.

Solar Cell Performance. Figure 6 compares the photocurrent density−voltage ($J-V$) properties of NT-based DSSCs incorporating 6.1 μm thick films that were cleaned and then dried as-deposited by either method A1 (H_2O/air-dried) or method A3 (ethanol/scCO_2-dried). No effort was made to optimize the performance of either cell. The DSSC incorporating a bundle-free and crack-free NT film processed using method A3 displayed better $J-V$ characteristics than the DSSC containing a film with severe clusters of NT bundles and microcracks processed using method A1. The photoresponse of the DSSC with the more ordered films exhibited a short-circuit photocurrent density (J_{sc}) of 5.7 mA/cm^2, an open-circuit photovoltage (V_{oc}) of 0.58 V, and a fill factor (FF) of 0.56 to give a solar conversion efficiency $\eta = 1.9\%$. In contrast, the DSSC with the less ordered film showed a J_{sc} of 4.9 mA/cm^2, V_{oc} of 0.60 V, and a FF of 0.53 to yield $\eta = 1.6\%$. Considering the small differences in V_{oc} and FF between the two cells, we attribute the 19% greater solar conversion efficiency of the ethanol/scCO_2-dried NT-based DSSC to mainly the 16% higher J_{sc}. The difference in J_{sc} can be accounted for in terms of the expression: $J_{sc} = q\eta_{lh}\eta_{inj}\eta_{cc}I_0$, where q is the elementary charge, η_{lh} is the light-harvesting efficiency, and η_{inj} is the charge-injection efficiency.[44] One can reasonably assume that the η_{inj} of the dye (N719) used for both DSSCs are the same because treating a preannealed film with either method A1 or A3 is unlikely to alter the nature of the dye-adsorption sites. Therefore, inasmuch as the charge-collection efficiencies of the cells, as discussed above, are approximately the same, we conclude that the higher J_{sc} and η of the DSSC with the ethanol/scCO_2-dried film are due to a larger η_{lh} owing to the larger internal surface area (23%) of the film and, correspondingly, to greater dye loading.

In summary, architectural disorder, resulting from bundling of nanotubes and microcracks in oriented TiO_2 arrays, significantly affects charge transport and recombination in DSSCs. Capillary forces that arise during evaporative drying of wetted NT films from the postgrowth cleaning step produce clusters of NT bundles and microcracks, the extent of which depended on the film thickness and surface tension of the cleaning solvent. Removal of liquids from the mesopores of the arrays by the supercritical CO_2 drying technique yielded bundle-free and crack-free NT films. Comparison of ethanol/scCO_2- and H_2O/air-dried films revealed that preventing morphological disorder induced by capillary stress can enhance significantly the total surface area of a film accessible to dye molecules. Electron transport is significantly faster in the ethanol/scCO_2-dried film than in the water/air-dried film. The intertube contacts that form within a NT bundle changes the transport mechanism from the expected one-dimensional pathway to a mixture of one- and three-dimensional pathways. One-dimensional transport shortens the transport pathway and reduces multiple electron-trapping events. Similar mechanistic effects are expected in other materials and devices consisting of nominally one-dimensional architectures (e.g., nanowire arrays). Changes in spatial dimensionality also affect recombination, but to a lesser degree than transport. Removing structural disorder reduces the density of recombination centers. The solar conversion efficiency is higher for architecturally ordered DSSCs than for the disordered ones owing to a higher short-circuit photocurrent resulting from a greater dye loading associated with a larger internal film surface area.

Acknowledgment. This work was supported by the Office of Science, Division of Chemical Sciences (A.J.F. and K.Z.), and the Office of Utility Technologies, Division of Photovoltaics (NRN), U.S. Department of Energy, under contract DE-AC36-99GO10337.

References

(1) O'Regan, B.; Grätzel, M. *Nature* **1991**, *353*, 737.
(2) Benkstein, K. D.; Kopidakis, N.; van de Lagemaat, J.; Frank, A. J. *J. Phys. Chem. B* **2003**, *107*, 7759.
(3) van de Lagemaat, J.; Benkstein, K. D.; Frank, A. J. *J. Phys. Chem. B* **2001**, *105*, 12433.
(4) Kopidakis, N.; Schiff, E. A.; Park, N. G.; van de Lagemaat, J.; Frank, A. J. *J. Phys. Chem. B* **2000**, *104*, 3930.
(5) Dittrich, T.; Lebedev, E. A.; Weidmann, J. *Phys. Status Solidi A* **1998**, *165*, R5.
(6) Forro, L.; Chauvet, O.; Emin, D.; Zuppiroli, L.; Berger, H.; Levy, F. *J. Appl. Phys.* **1994**, *75*, 633.
(7) Cao, F.; Oskam, G.; Meyer, G. J.; Searson, P. C. *J. Phys. Chem.* **1996**, *100*, 17021.
(8) de Jongh, P. E.; Vanmaekelbergh, D. *Phys. Rev. Lett.* **1996**, *77*, 3427.
(9) Nelson, J.; Haque, S. A.; Klug, D. R.; Durrant, J. R. *Phys. Rev. B* **2001**, *63*, 205321.

(10) Schlichthörl, G.; Park, N. G.; Frank, A. J. *J. Phys. Chem. B* **1999**, *103*, 782.
(11) Dloczik, L.; Ileperuma, O.; Lauermann, I.; Peter, L. M.; Ponomarev, E. A.; Redmond, G.; Shaw, N. J.; Uhlendorf, I. *J. Phys. Chem. B* **1997**, *101*, 10281.
(12) Solbrand, A.; Lindstrom, H.; Rensmo, H.; Hagfeldt, A.; Lindquist, S. E.; Sodergren, S. *J. Phys. Chem. B* **1997**, *101*, 2514.
(13) Bisquert, J.; Vikhrenko, V. S. *J. Phys. Chem. B* **2004**, *108*, 2313.
(14) Baxter, J. B.; Aydil, E. S. *Appl. Phys. Lett.* **2005**, *86*, 053114.
(15) Law, M.; Greene, L. E.; Johnson, J. C.; Saykally, R.; Yang, P. D. *Nat. Mater.* **2005**, *4*, 455.
(16) Galoppini, E.; Rochford, J.; Chen, H. H.; Saraf, G.; Lu, Y. C.; Hagfeldt, A.; Boschloo, G. *J. Phys. Chem. B* **2006**, *110*, 16159.
(17) Martinson, A. B. F.; McGarrah, J. E.; Parpia, M. O. K.; Hupp, J. T. *Phys. Chem. Chem. Phys.* **2006**, *8*, 4655.
(18) Macak, J. M.; Tsuchiya, H.; Ghicov, A.; Schmuki, P. *Electrochem. Commun.* **2005**, *7*, 1133.
(19) Mor, G. K.; Shankar, K.; Paulose, M.; Varghese, O. K.; Grimes, C. A. *Nano Lett.* **2006**, *6*, 215.
(20) Wang, H.; Yip, C. T.; Cheung, K. Y.; Djurisic, A. B.; Xie, M. H.; Leung, Y. H.; Chan, W. K. *Appl. Phys. Lett.* **2006**, *89*, 023508.
(21) Zhu, K.; Neale, N. R.; Miedaner, A.; Frank, A. J. *Nano Lett.* **2007**, *7*, 69.
(22) Varghese, O. K.; Gong, D. W.; Paulose, M.; Grimes, C. A.; Dickey, E. C. *J. Mater. Res.* **2003**, *18*, 156.
(23) Mor, G. K.; Shankar, K.; Paulose, M.; Varghese, O. K.; Grimes, C. A. *Nano Lett.* **2005**, *5*, 191.
(24) Macak, J. M.; Tsuchiya, H.; Taveira, L.; Aldabergerova, S.; Schmuki, P. *Angew. Chem., Int. Ed.* **2005**, *44*, 7463.
(25) Macak, J. M.; Tsuchiya, H.; Schmuki, P. *Angew. Chem., Int. Ed.* **2005**, *44*, 2100.
(26) Cai, Q. Y.; Paulose, M.; Varghese, O. K.; Grimes, C. A. *J. Mater. Res.* **2005**, *20*, 230.
(27) Paulose, M.; Shankar, K.; Yoriya, S.; Prakasam, H. E.; Varghese, O. K.; Mor, G. K.; Latempa, T. A.; Fitzgerald, A.; Grimes, C. A. *J. Phys. Chem. B* **2006**, *110*, 16179.
(28) Ruan, C. M.; Paulose, M.; Varghese, O. K.; Mor, G. K.; Grimes, C. A. *J. Phys. Chem. B* **2005**, *109*, 15754.
(29) Shankar, K.; Mor, G. K.; Fitzgerald, A.; Grimes, C. A. *J. Phys. Chem. C* **2007**, *111*, 21.
(30) Fan, J. G.; Dyer, D.; Zhang, G.; Zhao, Y. P. *Nano Lett.* **2004**, *4*, 2133.
(31) Zhao, Y. P.; Fan, J. G. *Appl. Phys. Lett.* **2006**, *88*, 103123.
(32) Neale, N. R.; Kopidakis, N.; van de Lagemaat, J.; Grätzel, M.; Frank, A. J. *J. Phys. Chem. B* **2005**, *109*, 23183.
(33) Schlichthörl, G.; Huang, S. Y.; Sprague, J.; Frank, A. J. *J. Phys. Chem. B* **1997**, *101*, 8141.
(34) van de Lagemaat, J.; Park, N. G.; Frank, A. J. *J. Phys. Chem. B* **2000**, *104*, 2044.
(35) Kralchevsky, P. A.; Paunov, V. N.; Denkov, N. D.; Ivanov, I. B.; Nagayama, K. *J. Colloid Interface Sci.* **1993**, *155*, 420.
(36) Hearn, E. J. *Mechanics of Materials*, 3rd ed.; Butterworth-Heinemann: Woburn, MA, 1997; Vol. 1.
(37) Kataoka, S.; Anderson, M. A. *Thin Solid Films* **2004**, *446*, 232.
(38) Yang, T. S.; Shiu, C. B.; Wong, M. S. *Surf. Sci.* **2004**, *548*, 75.
(39) Wang, R.; Sakai, N.; Fujishima, A.; Watanabe, T.; Hashimoto, K. *J. Phys. Chem. B* **1999**, *103*, 2188.
(40) van de Lagemaat, J.; Frank, A. J. *J. Phys. Chem. B* **2001**, *105*, 11194.
(41) Zhu, K.; Kopidakis, N.; Neale, N. R.; van de Lagemaat, J.; Frank, A. J. *J. Phys. Chem. B* **2006**, *110*, 25174.
(42) Kopidakis, N.; Neale, N. R.; Zhu, K.; van de Lagemaat, J.; Frank, A. J. *Appl. Phys. Lett.* **2005**, *87*, 202106.
(43) Kopidakis, N.; Benkstein, K. D.; van de Lagemaat, J.; Frank, A. J. *J. Phys. Chem. B* **2003**, *107*, 11307.
(44) Frank, A. J.; Kopidakis, N.; van de Lagemaat, J. *Coord. Chem. Rev.* **2004**, *248*, 1165.

NL072145A